

Article

Nickel Glycerolate Overcoming a High-Entropy Configuration for High-Performance Oxygen Evolution Reaction

Irlan S. Lima ¹, Rafael S. Pereira ² , Timothy G. Ritter ³, Reza Shahbazian-Yassar ⁴ , Josué M. Gonçalves ^{1,4,*} 
and Lúcio Angnes ^{1,*}

¹ Instituto de Química, Universidade de São Paulo, Av. Prof. Lineu Prestes 748, São Paulo 05508-000, SP, Brazil; irlan.santos@usp.br

² Centro de Engenharia, Modelagem e Ciências Sociais Aplicadas, Universidade Federal do ABC, Santo André 09210-580, SP, Brazil; p.rafael@ufabc.edu.br

³ Department of Civil & Materials Engineering, University of Illinois Chicago, Chicago, IL 60607, USA; tritter2@uic.edu

⁴ Department of Mechanical and Industrial Engineering, University of Illinois Chicago, Chicago, IL 60607, USA; rsyassar@uic.edu

* Correspondence: josuefiscoquimico@hotmail.com (J.M.G.); luangnes@iq.usp.br (L.A.)

Abstract: In response to the requirement for alternative energy conversion and storage methods, metal-glycerolates (MG) and their analogs are considered promising classes of electrode material that can be synthesized in various designs. Recently, the concept of high-entropy configuration and multimetallic systems has gained attention in the field of electrocatalysis. In fact, the presence of five or more metals in a single-phase material can produce unique and unexpected properties. Thus, it becomes crucial to explore different metal combinations and evaluate their synergistic interaction as a result of these combinations. Therefore, in this work, a scalable solvothermal method was used to synthesize a high-entropy glycerolate (HEG) containing Ni, Zn, Mn, Mg, and Co ions (HEG) and their respective sub-systems such as NiG, NiMnG, and NiMnZnG. The SEM-EDS images showed the excellent distribution of the metal cations in the obtained microspheres. Surprisingly, our experiments demonstrated that even in reaching a single-phase HEG, the oxygen evolution reaction (OER) performance measured in 1 M KOH electrolyte did not surpass the benefit effect observed in the NiG-based carbon paste with an overpotential of 310 mV (@10 mA cm⁻²), against 341 mV (@10 mA cm⁻²) of HEG. Moreover, the NiG shows good stability toward OER even after 24 h, which is attributed to the NiOOH active phase generated during the electrochemical cycling.

Keywords: metal-glycerolate; high-entropy coordination compound; water-splitting; oxygen evolution reaction



Citation: Lima, I.S.; Pereira, R.S.; Ritter, T.G.; Shahbazian-Yassar, R.; Gonçalves, J.M.; Angnes, L. Nickel Glycerolate Overcoming a High-Entropy Configuration for High-Performance Oxygen Evolution Reaction. *Catalysts* **2023**, *13*, 1371. <https://doi.org/10.3390/catal13101371>

Academic Editors: Indra Neel Pulidindi, Thirukkallam Kanthadai Varadarajan and Balasubramanian Viswanathan

Received: 11 September 2023

Revised: 2 October 2023

Accepted: 13 October 2023

Published: 16 October 2023



Copyright: © 2023 by the authors. Licensee MDPI, Basel, Switzerland. This article is an open access article distributed under the terms and conditions of the Creative Commons Attribution (CC BY) license (<https://creativecommons.org/licenses/by/4.0/>).

1. Introduction

The high and growing energy consumption of modern society results in increased environmental pollution, thus urging the expansion of clean and renewable energy technologies, such as those based on solar energy and water, via photoinduced water-splitting [1]. The decomposition of water requires two half-cells, which give rise to the oxygen evolution reaction (OER) and hydrogen evolution reaction (HER) at the anode and cathode, respectively. It is well known that OER involves a tetra-protonic and tetra-electronic reaction mechanism characterized by sluggish reaction kinetics. Therefore, advanced catalysis based on earth-abundant metal materials is highly desirable as an alternative to overcome the higher activation barrier, which can establish a connection between renewable electricity and chemical fuels [2,3].

Thus, several classes of electrode materials based on transition metals, such as metal oxides [4], metal hydroxides [5], metal phosphides [6], metal sulfides [7], and metal-organic frameworks (MOFs) [8] have been studied as an alternative to precious metals-based

catalysts, such as iridium (IrO_2) and ruthenium (RuO_2) oxides. In addition, it is essential to mention the conversion to corresponding metal oxyhydroxides (M-OOH), known as key species for electrocatalytic activity. In fact, under OER conditions in an alkaline medium, the detailed spectroscopic analysis of the metals before and after the OER, as well as in situ analysis during OER and postmortem analysis performed on post-OER electrocatalyst, confirmed the formation of M-OOH , as reported in many works [9]. As a result, it was confirmed that the catalytic activity significantly depends on the chemical composition and the surface electronic design [10].

In recent years, multimetal-based materials have been considered a new family of catalysts for the next generation of electrode materials in electrocatalysis. Moreover, recent advancements underscore the trend toward the continual development of novel high-entropy materials (HEMs) constructed by five or more elements [9]. In fact, HEMs are characterized by their complex compositions and structures involving multiple elements, which usually offer several advantages in catalytic applications such as enhanced activity, selectivity, stability, and durability, as well as tunable properties, resistance to deactivation, novel reaction pathways and multi-functionality. In addition, the countless possibilities of combinations proportioned by the HEMs provide a vast field to manipulate the electronic structure in order to enhance the catalytic effects. In fact, the concept of HEMs has opened up new avenues for materials scientists and engineers to explore unconventional compositions and achieve exceptional properties in a wide range of materials, such as high-entropy alloys (HEAs) [11], high-entropy oxides (HEOs) [11,12], and high-entropy hydroxides (HEHs) [12]. This concept represents a departure from traditional material design principles and continues to be an exciting and evolving field in materials science in diverse types of catalytic reactions [13]. Recently, the concept of high entropy was introduced into some coordination compounds (high-entropy coordination compounds—HE-CCs) such as Prussian blue analogues (PBAs), metal–organic frameworks (MOFs), and metal-glycerolates (MG), as well as metal-polyphenol coordination polymers [9]. These novel HE-CCs hold the potential for tailored applications and innovative solutions [9].

Among HE-CCs, high-entropy metal-glycerolates (HEG) and their lower-entropy metal-glycerolates analogues have received considerable attention as an emerging type of coordination polymer (inorganic-organic) [14,15]. In particular, metal-glycerolates possess a layered structure, which is based on stacked metal–oxygen sheets separated by glycerolate anions [16]. This feature is analogous to well-known anion-intercalated metal hydroxides, which allow fast transport of the reactants to the material, thus optimizing the availability of catalyst active sites and favoring the formation of the $-\text{OOH}$ group that is expected under OER conditions [14]. However, an intermediate pursuing an M-O bond is expected to be formed during OER. Consequently, the adsorbed species should bind to the surface neither too strongly nor too weakly for an efficient electroactivity, as says the Sabatier principle [17]. Therefore, the impact of creating a synergistic design becomes critical for high-performance multimetal-based OER electrocatalysis.

On the other hand, carbon materials are an interesting choice as conductive substrates due to their low cost, high stability, and good electronic conductivity. In addition, the carbon substrate plays a crucial role in acting synergistically with the electrocatalyst, enhancing catalytic activity as well as their beneficial properties for oxygen desorption and infiltration of the electrolyte [18].

Motivated by the aforementioned considerations, it is important to highlight the recent development of new electrode materials derived from metal-glycerolates as well as their applicability in energy conversion and storage. The use of glycerol is advantageous since it is a by-product generated in large quantities in the production of biodiesel [19]. Thus, in this work, we evaluate the performance of a new high-entropy metal-glycerolate (HEG) containing Ni, Zn, Mn, Mg, and Co using a carbon paste electrode (CPE). Surprisingly, the monometallic NiG exhibited the lowest overpotential of 310 mV (@10 mA cm^{-2}), while the HEG presented 341 mV (@10 mA cm^{-2}), being close to the trimetallic NiMnZnG and bimetallic NiMnG. In fact, these results demonstrate that attaining a high-entropy

configuration within a single-phase material does not necessarily ensure an optimized catalytic system. The good performance of NiG was attributed to the presence of the NiOOH active sites in the CPE-based electrode, increasing the conductivity of the catalytic sites. Along with the experiments, it was observed that the presence of Mg in HEG may be responsible for the passivation of the HEG-modified CPE. The excessive presence of Zn and Mn does not provide an effective synergic effect when combined with nickel-glycerolate, which contains a highly active NiOOH under OER conditions.

2. Results and Discussion

2.1. Physicochemical Characterization

The metal-glycerolate crystalline structure of the as-prepared materials was first investigated by XRD measurements. As expected, all the specimens exhibit a very similar pattern, as shown in Figure 1a. The presence of typical diffraction peaks at 10.5° , 35.6° , and 60.8° consists of stacked metal–oxygen sheets separated by bonded glycerolate anions which belong to the metal alkoxides group with glycerol acting as solvent and reagent, simultaneously [20,21]. The low-angle peak (10.50°) is related to the interlayer space, which, in this instance, is ~ 0.84 nm. Nonetheless, some unique features can be observed in the diffraction pattern of NiMnZnG, specifically, the peaks located at $2\theta = 16.90^\circ$, 20.60° , and 27.45° , which indicate the crystal phase of Zn-monoglycerolate (JCPDS card No. 00-23-1975) [22]. Therefore, an amount of zinc acetate as high as 33.33% can result in the segregation of a stable Zn-rich metal-glycerolate phase, as observed for the NiMnZnG XRD pattern.

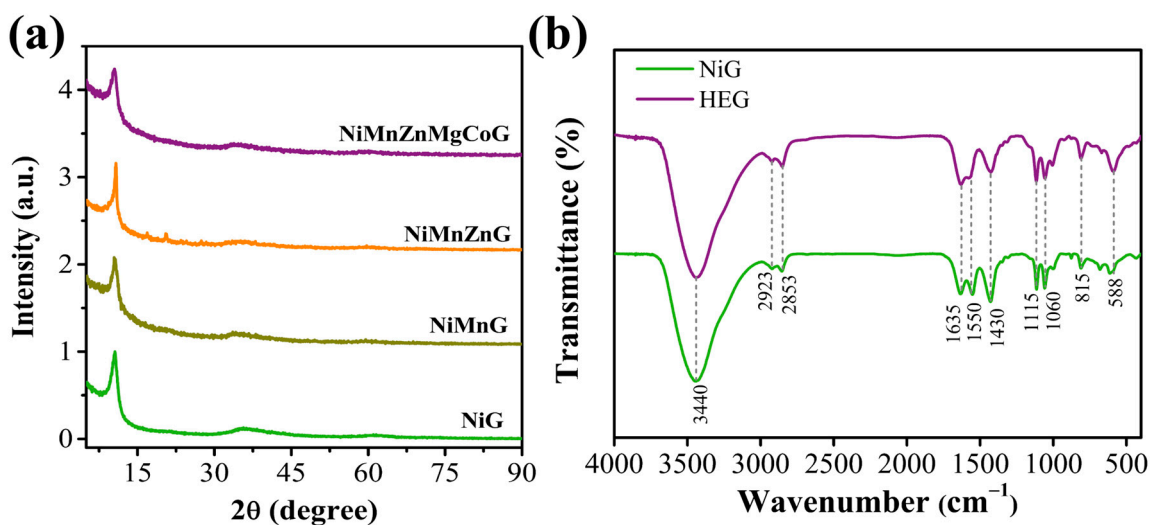


Figure 1. (a) XRD pattern of NiMnZnMgCoG, NiMnZnG, NiMnG, and NiG and (b) FTIR spectra of NiG and HEG specimens.

Further, to determine the molecular structure of the samples, Fourier transform infrared spectroscopy (FTIR) was applied. The FTIR spectra of NiG and HEG (Figure 1b) contain many bands related to organic compounds due to the intrinsic presence of glycerol-based compounds. The band centering at 3440 cm^{-1} corresponds to the stretching vibrations of hydroxyl groups (O–H), which can be related to the functional groups of glycerolate anions. The bands centered at 2924 and 2855 cm^{-1} are attributed to anti-symmetric methylene groups ($-\text{CH}_2$) and symmetric C–H stretching modes, respectively. Meanwhile, the C–H bending modes can be observed in the low-intensity IR absorption shoulder at 1350 cm^{-1} [20,23]. The peaks appearing in the 950 and 1060 cm^{-1} range were attributed to the C–O stretching vibrations, whereas the peak at 815 cm^{-1} is related to the out-of-plane C–H bending vibrations. In addition, the IR band at 588 cm^{-1} is assigned to the metal–oxygen bond (M–O) stretching modes, which suggests the formation of the metal-glycerolates [24]. Moreover, the bands between 1430 and 1550 cm^{-1} were assigned to the O–C–O stretching vibration modes, while the one centered at 1635 cm^{-1} can be related

to the C=C stretching mode. These bands emerge as a consequence of glycerol oxidation reactions that can occur during the solvothermal reaction [25,26].

The decomposition process of NiG and HEG was analyzed via TGA in an atmosphere of synthetic air (Figure S1a). It is widely known that coordination compounds, which combine organic and inorganic constituents, undergo decomposition at temperatures around 300 °C, leading to the corresponding metal oxide formation, as reported in our previous work [27]. The TGA curve of NiG indicates four major processes. The first is related to removing absorbed water and degrading oxygen-containing organic groups with a weight loss of ~43%. In the range of 235 and 275 °C occurs a second process with a weight loss of ~32% due to thermal decomposition of glycerolate ligands. The third process, related to the formation of the oxide phase, is observed in the range of 275 and 420 °C. Lastly, a mass increase surrounding 420 to 800 °C results from the oxidation process of metal elements in the presence of air [27], as well as the persistence of carbon residues, even following exposure to temperatures as elevated as 800 °C [27]. A similar pattern was registered for the HEG (Figure S1b).

SEM (Figure 2) imaging was utilized to scrutinize the morphology of the NiG, NiMnZnG, and HE-Gly particles synthesized in this study. In general, the collected SEM backscattered electrons (BSE, Figure 2a–f) and secondary electron images (SE, Figure 2g–i) reveal the spherical morphology with interconnected microparticles.

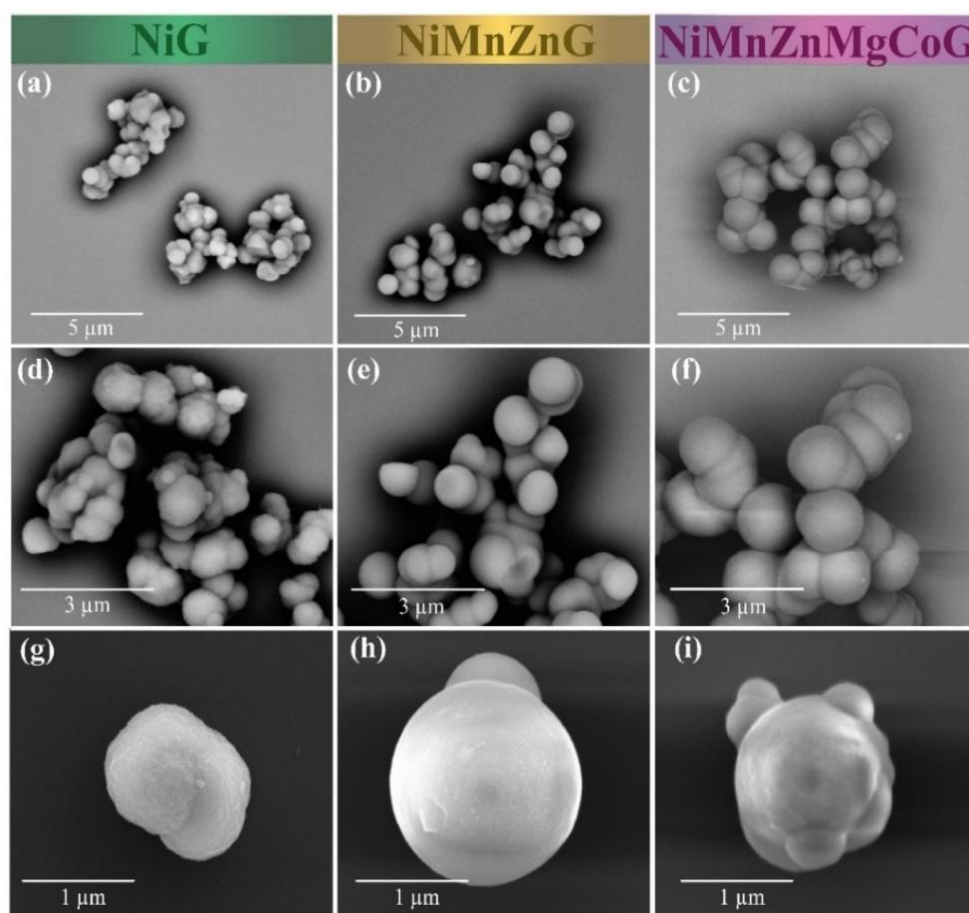


Figure 2. SEM images showing the microspheres of (a,d,g) NiG, (b,e,h) NiMnZnG, and (c,f,i) HEG in different magnifications. From (a–f), the images were collected in BSE mode, while (g–i) corresponds to SE mode. Their corresponding magnifications are (a–c) $\times 6200$, (d–f) $\times 12,000$, and (g–i) $\times 31,000$.

The SEM-EDS elemental analysis verified the composition of the metal-glycerolates particles, as shown in Figure 3. The NiG SEM-EDS layered image and the uniform elemental distribution mapping of C, O, and Ni elements are represented in Figures 3a and S2. For

a complex glycerolate such as the HEG, the SEM-EDS layered elemental mapping also indicated the uniform distribution of Ni, Zn, Mn, Mg, and Co ions in the glycerol-based matrix (Figure 3c), as expected for a well-behaved high-entropy coordination compound. In fact, comparable elemental distributions are discernible in other areas as well (Figure S3), affirming the effectiveness of the solvothermal route as a robust strategy in the design of HEGs. Such a homogeneous factor was also seen in the NiMnZnG specimen. However, as depicted in Figure S4, it is also possible to identify regions abundant in Mn and Zn, thereby validating the presence of phase segregation consistent with the XRD analysis. Furthermore, to confirm the metal concentrations of HEG and their lower entropy analogs, ICP-OES measurements were performed, revealing that all metal-glycerolates contain nearly equimolar amounts of metal ions, as summarized in Table 1.

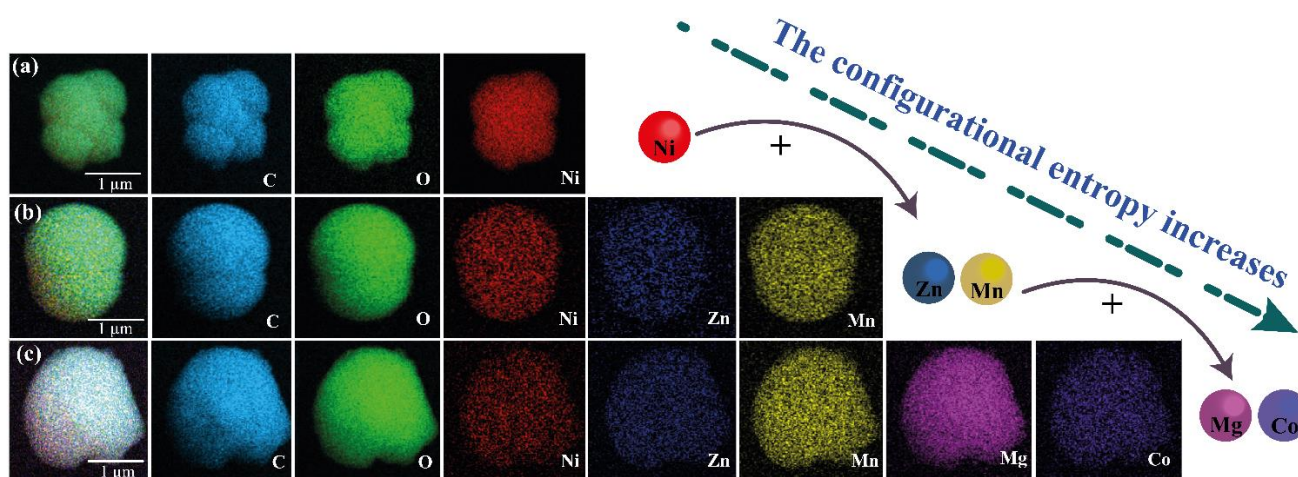


Figure 3. SEM-EDS mapping showing the microspheres of (a) NiG, (b) NiMnZnG, and (c) HEG microspheres. Carbon (light blue), oxygen (green), nickel (red), zinc (blue), manganese (yellow), magnesium (magenta), and cobalt (lilac). Magnification of $\times 20,000$.

Table 1. Chemical composition (atomic %) obtained from ICP-OES.

Material	Ni (At%)	Mn (At%)	Zn (At%)	Mg (At%)	Co (At%)
NiG	100	-	-	-	-
NiMnG	51.20	48.79	-	-	-
NiMnZnG	32.78	33.17	34.05	-	-
NiMnZnMgCoG	19.36	21.65	20.01	18.21	20.74

The surface chemistry analysis of the synthesized samples was performed via X-ray photoelectron spectroscopy (XPS). The high-resolution XPS spectra of NiG, NiMnZnG, and HEG are shown in Figure 4. The survey spectra of NiG, NiMnZnG, and HEG are illustrated in Figure S5, and Figure S6 contains the survey spectrum and the high-resolution spectra of the NiMnG specimen. The Ni 2p spectrum for the NiG (Figure 4a) specimen shows two peaks at the Ni 2p_{3/2} region that confirms the presence of Ni²⁺ and Ni³⁺, where the corresponding peaks are seen at 854.50 eV and 856.30 eV, respectively.

The Ni 2p spectrum for the HEG compound shows similar features to the NiG previously mentioned. Additionally, the Mn 2p spectrum reveals two peaks at 642.60 eV and 654.60. The surface chemistry analysis of the synthesized samples was performed via X-ray photoelectron spectroscopy (XPS). The high-resolution XPS spectra of NiG, NiMnZnG, and HEG are shown in Figure 4. The survey spectra of NiG, NiMnZnG, and HE are illustrated in Figure S5, and Figure S6 contains the survey spectrum and the high-resolution spectra of the NiMnG specimen. The Ni 2p spectrum for the NiG (Figure 4a) specimen shows two peaks at the Ni 2p_{3/2} region that confirms the presence of Ni²⁺ and Ni³⁺, where the

corresponding peaks are seen at 854.50 eV and 856.30 eV, respectively [26]. The Ni 2p spectrum for the HEG compound shows similar features to the NiG previously mentioned. Additionally, the Mn 2p spectrum reveals two peaks at 642.60 eV and 654.60 eV, which correspond to Mn 2p_{3/2} and Mn 2p_{1/2}, respectively. The Mn 2p_{3/2} peak was deconvoluted in two peaks, Mn²⁺ at 640.60 eV and Mn³⁺ at 642.50 eV. The peak at 647.00 eV corresponds to a satellite peak [28]. These same profiles were observed for the NiMnG specimen (Figure S6).

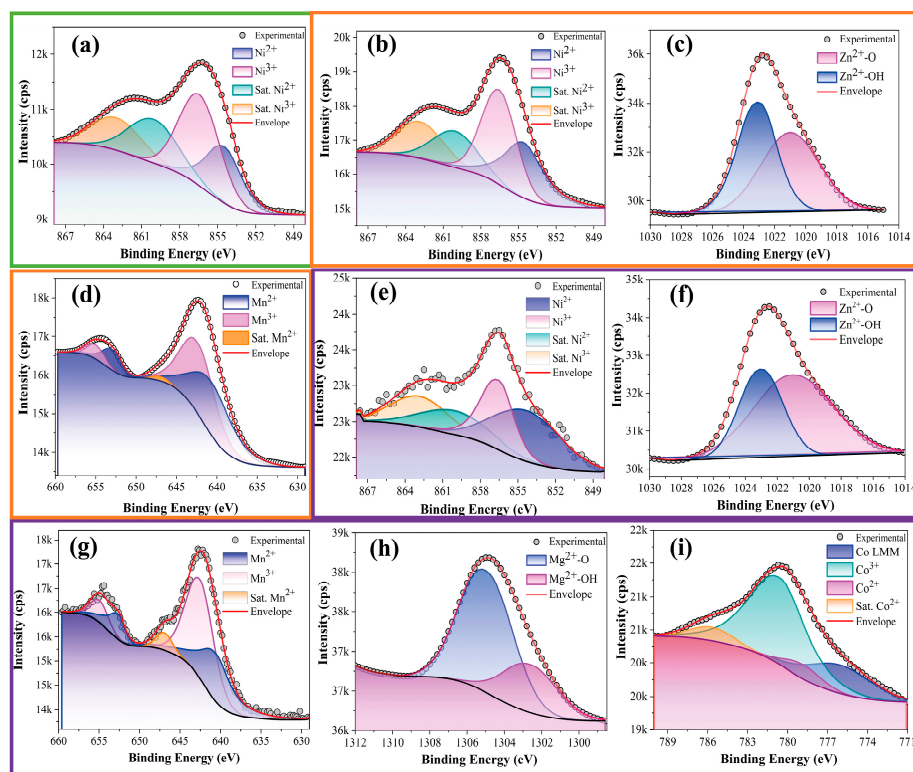


Figure 4. High-resolution XPS spectra for (a) NiG (Ni 2p), (b–d) NiMnZnG (Ni 2p, Zn 2p and Mn 2p), and (e–i) HEG (Ni 2p, Zn 2p, Mn 2p, Mg 1s, and Co 2p).

The Zn 2p spectrum was fitted into two peaks belonging to the Zn²⁺ valence state, which indicated the presence of Zn-O and Zn-OH bonding at 1021.00 eV and 1023.00 eV, respectively [1]. The Mg 1s spectrum was deconvoluted into two peaks assigned to the Mg²⁺ valence state, Mg-OH at 1302.58 eV and Mg-O at 1304.96 eV [27]. The Co 2p spectrum exhibited a Co 2p_{3/2} peak at 780.57 eV, which was deconvoluted into two main peaks at 778.77 eV (Co³⁺) and 780.55 eV (Co²⁺) [29]. The peak at 776.08 eV is assigned to Co LMM Auger emission, while the peak at 785.75 is assigned to a satellite peak. The Ni 2p, Mn 2p, and Zn 2p spectra (Figure 4b–d) for the NiMnZnG compound agree with the spectra collected for NiMnZnMgCoG as well. The O 1s spectrum for the HEG, as well as NiG and NiMnZnG (Figure S5g–i), was fitted in four peaks at 529.50 eV, 531.00 eV, 532.00 eV, and 533.05 eV, attributed to the oxygen lattice O–M, O–H, C–O, and C=O or physically absorbed water. Moreover, for the C 1s (Figure S5d–f) spectrum, the deconvoluted peaks at 284.00 eV, 284.80 eV, 286.09 eV, and 288.48 eV are designed to C=C, C–C, C–O, and C=O [27]. The presence of C=C is seen as a result of organic sub-products originating from glycerol oxidation, in agreement with the FTIR results.

2.2. Electrochemical Characterization

The electrocatalytic performance of metal-glycerolates modified CPE against OER was analyzed using the standard three electrode system in 1.0 M KOH solution. The LSV curves of NiG, NiMnG, NiMnZnG, and HEG are shown in Figure 5a. The monometallic NiG presented the best activity among all the materials, demanding an overpotential of

310 mV after 1000 CV cycles (Figure 5b), revealing the key role of in situ-formed NiOOH active phase for OER activity [30]. Furthermore, a potential of 1.587 V ($\eta_{10} = 357$ mV) and 1.574 V ($\eta_{10} = 344$ mV) at 10 mA cm^{-2} were registered for the bi- and trimetallic glycerolate modified CPE, respectively. These performances show that NiMnG in equimolar values exhibits a poor electrocatalytic effect toward OER. This finding aligns with the theoretical studies conducted by Zhao et al. [31], who, through a systematic screening for OER based on a surface edge-site model with exposed active sites for metal-hydroxides and metal-oxyhydroxides, suggested that MnOOH is a much less active OER catalyst when compared to NiOOH or CoOOH species.

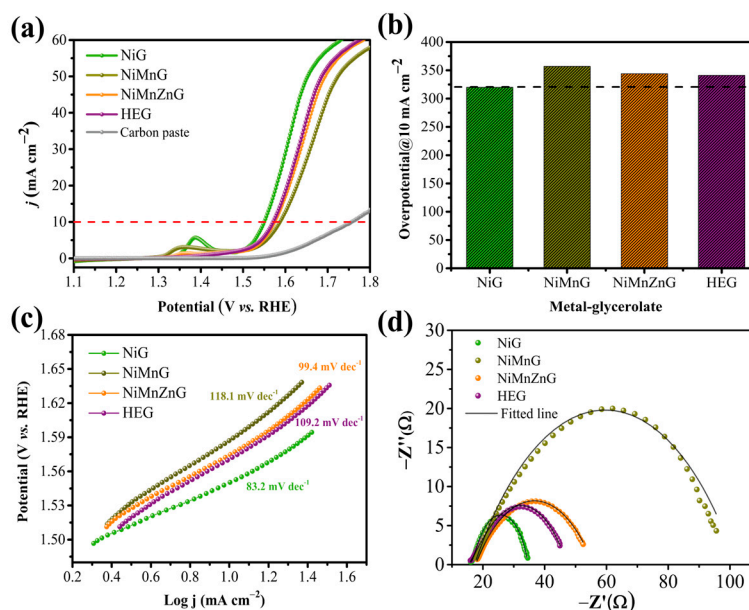


Figure 5. (a) LSV curves of glycerolates modified CPE prepared and the pure CPE collected at a scan rate of 5 mV s^{-1} in 1.0 M KOH electrolyte after 1000 CV cycles. (b) Overpotential at a current density of 10 mA cm^{-2} . (c) The Tafel plots of mono-, bi-, tri-, and high-entropy glycerolates. (d) Nyquist plots of glycerolates CPE at a potential of 1.573 V (vs. RHE) in 1.0 M KOH solution.

However, the activity of the trimetallic glycerolate surpasses that of NiMnG; this can be attributed to the proper incorporation of Zn^{2+} species, which may result in a partial charge transfer to the Ni sites, thereby boosting the electronic conductivity of the electrode [32]. In the case of the high-entropy NiMnZnMgCoG modified CPE, the additions of Mg and Co result in an overpotential of $\eta_{10} = 341$ mV, which are indistinguishable from NiMnZnG. The activity of HEG, when compared to the NiMnG or NiMnZnG, could be attributed only to the presence of cobalt cations; that is, the active CoOOH phase in situ generated plays a crucial role in OER electroactivity [31,33]. Nevertheless, the monometallic NiG still exhibits the best performance as a consequence of plenty of NiOOH active sites in CPE-based electrode. In fact, these metal oxyhydroxides derived from metal-glycerolates are very likely to be the real intrinsic active species for the OER, as confirmed in the literature using various in situ and ex situ analyses [1,20]. The results obtained in the present study demonstrate comparability with or even surpass the performance of numerous reference transition metal oxides, metal hydroxides, and metal-glycerolates, as can be seen in Table 2. In addition, these results also corroborate that the CPE can be used as a great conductive platform for this kind of study.

The results obtained in the current study demonstrate comparability with or even surpass the performance of numerous transition metal oxides and metal hydroxides.

For the investigation of the kinetics of the metal-glycerolate electrocatalysts, the Tafel slope was determined. The curves in Figure 5c illustrate that NiG has the smallest value of Tafel slope, corresponding to 83.2 mV dec^{-1} , followed by NiMnZnG ($104.8 \text{ mV dec}^{-1}$), HEG ($109.2 \text{ mV dec}^{-1}$), and NiMnG ($118.1 \text{ mV dec}^{-1}$). These results indicate the superior

kinetics of NiG for OER, corroborating with the overpotential values. Alongside the performance of electrocatalytic OER activity of metal-glycerolates samples, electrochemical impedance spectroscopy (EIS) was carried out. The Nyquist plots measured at 1.573 V (vs. RHE) are shown in Figure 5d; the plots were fitted according to the simplified Randles cell [34]. As expected, the charge-transfer resistance (R_{ct}) for NiG (18.5 Ω), NiMnG (84.7 Ω), NiMnZnG (37.9 Ω), and HEG (32.4 Ω) agree with the OER performances. Following the same sequence, the resistance of solution fitted for NiG, NiMnG, NiMnZnG and HEG were 16.5 Ω , 17.3 Ω , 17.7 Ω , and 16.0 Ω . Therefore, the NiG yields the lowest R_{ct} followed by HEG; thus, both metal-glycerolates are the most efficient for charge transport during OER.

Table 2. Comparison of catalytic performance with other reported works.

Electrocatalyst	Substrate	η_{10} (mV @ ten mA cm^{-2})	Tafel Slope (mV dec^{-1})	Stability (Hr)	Electrolyte	Ref.
IrO ₂	GCE	380	83	-	1.0 M KOH	[35]
RuO ₂	GCE	350	106	-	1.0 M KOH	[35]
Ni ₆ Co ₁₁ Mn-LDH	GCE	248	72.2	22 ($j = 100 \text{ mA cm}^{-2}$)	1.0 M KOH	[36]
CrMnFeCoNiTiZn-glycerolate	Ni foam	251	42.3	60	1.0 M KOH	[1]
Mn-Co-P	GCE	η_{50} (50 mA cm^{-2}) 330	59	8	1.0 M KOH	[37]
Ni ₂ Zn _{0.5} Fe-LDH	CPE	370	16	13	Buffer pH = 7	[32]
NiMn-DLH	GCE	296	102	24	1.0 M KOH	[31]
NiCo-Fe LDH	GCE	285	62	12	1.0 M KOH	[38]
CoCuFe-Gly	GCE	317	69	69	1.0 M KOH	[39]
NiMnZnMgCoG	CPE	342	83.2	24	1.0 M KOH	This work
NiG	CPE	310	109.2	24	1.0 M KOH	This work

Analyzing the CVs during 1000 cycles can aid in comprehending the electrochemical behavior of the metal-glycerolates. Extended periods of cycling are known to cause a shift of the anodic potential peak of nickel-containing species, such as metal oxides and metal hydroxides. As shown in Figure S7, the NiG exhibited the largest shift of the anodic wave compared to NiMnG and NiMnZnG. This shift is linked to the transformation of Ni(OH)₂ to NiOOH [26]. This phenomenon may explain the superior behavior of this monometallic glycerolate since it is more difficult to oxidize NiO_xH_y species, as evidenced by the anodic shift of the Ni^{2+/3+} oxidation peak. Hence, this provides greater oxidizing power and favorable kinetics for OER.

Moreover, it is well known that amorphous materials supply more active sites, thus favoring the charge transfer reactions [33]. This local amorphous structure acts as an accelerator for the formation of intermediates, being a crucial factor in the OER performance [20,40]. To exemplify this, the NiG and HEG samples were annealed at 800 °C for 3 h in order to form their respective metal oxides as described by Gonçalves et al. [27]. As expected, the XRD patterns (Figure S8) indicate that thermal treatment increases the crystallinity, as it was predicted for the formation of metal-glycerolates-derived metal oxides. Likewise, the HEG undergoes a process that generates a porous high-entropy oxide (HEO) based on spinel (NiMnZnMgCo)₃O₄ crystals structure (Fd-3 m space group) containing segregated MgO phase (JCPDS Card No. 45-0946) with a space group of Fm-3 m (Figure 6), whereas the thermal treatment of NiG originates nickel oxide (NiO, JCPDS Card No. card 04-0835) (Figure S9).

Interestingly, the OER performance drastically reduces with the annealing process, as illustrated by LSV curves in Figure 7a, demonstrating the superior performance of coordination compounds as electrocatalysts for oxidation reactions. Moreover, the NiG and HEG-modified carbon paste electrocatalysts were finally examined for stability. Figure 7b

shows the 24 h chronopotentiometry test at $j = 10 \text{ mA cm}^{-2}$. The analyzed metal-glycerolates did not exhibit drastic changes even after 24 h, proving that the respective materials were remarkably steady during the OER. In addition, the LSVs collected after 100, 500, and 1000 redox cycles (Figure S10) indicate the formation of active sites even after prolonged cycling periods, which supports the findings of the stability test.

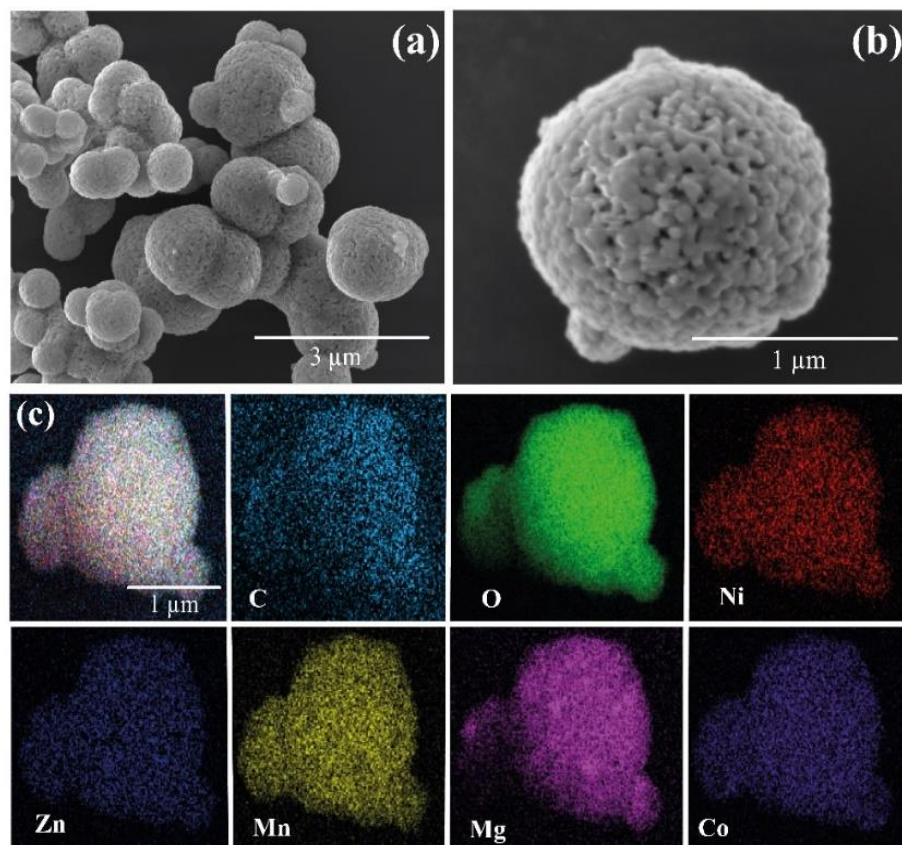


Figure 6. (a,b) SEM images of HEO. (c) SEM-EDS mappings of HEO. Carbon (light blue), oxygen (green), nickel (red), zinc (blue), manganese (yellow), magnesium (magenta), and cobalt (lilac). With magnification of (a) $\times 14,000$, (b) $\times 50,000$, and (c) $\times 31,000$.

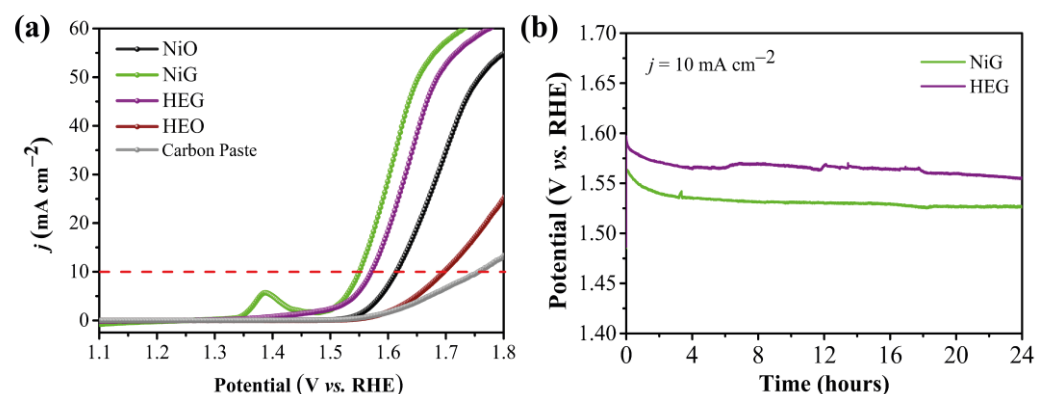


Figure 7. (a) LSV Comparison between glycerolates modified CPEs and their respective metal oxides, as well as the pure carbon paste at a scan rate of 5 mV s^{-1} in 1.0 M KOH electrolyte. (b) Chronopotentiometry measurement of NiG and HEG at 10 mA cm^{-2} for 24 h.

3. Materials and Methods

3.1. Chemicals

All reagents employed in this work were of analytical grade and were utilized without further purification. Nickel acetate tetrahydrate ($\text{Ni}(\text{CH}_3\text{COO})_2 \cdot 4\text{H}_2\text{O}$) was acquired from Sigma-Aldrich. Cobalt acetate tetrahydrate ($\text{Co}(\text{CH}_3\text{COO})_2 \cdot 4\text{H}_2\text{O}$), magnesium acetate tetrahydrate ($\text{Mg}(\text{CH}_3\text{COO})_2 \cdot 4\text{H}_2\text{O}$), and zinc acetate dihydrate ($\text{Zn}(\text{CH}_3\text{COO})_2 \cdot 2\text{H}_2\text{O}$), glycerin, isopropyl alcohol, ethyl alcohol, and potassium hydroxide were obtained from Synth, whereas manganese acetate tetrahydrate ($\text{Mn}(\text{CH}_3\text{COO})_2 \cdot 4\text{H}_2\text{O}$) was purchased from Carlo Erba (Milano, Italy). To prepare modified carbon paste electrodes, we utilized graphite powder (Acheson-38) obtained from Fisher and mineral oil purchased from Sigma-Aldrich (St. Louis, MO, USA). All aqueous solutions were prepared with ultrapure deionized water from a MilliQ purification system (DI-water, $\rho = 18.2 \text{ M}\Omega \text{ cm}$).

3.2. Synthesis

A one-step solvothermal method was used to produce high-entropy glycerolate microspheres and their lower-entropy metal-glycerolates analogues. Generally, equimolar $\text{Ni}(\text{CH}_3\text{COO})_2 \cdot 4\text{H}_2\text{O}$, $\text{Co}(\text{CH}_3\text{COO})_2 \cdot 4\text{H}_2\text{O}$, $\text{Mn}(\text{CH}_3\text{COO})_2 \cdot 4\text{H}_2\text{O}$, $\text{Mg}(\text{CH}_3\text{COO})_2 \cdot 4\text{H}_2\text{O}$, and $\text{Zn}(\text{CH}_3\text{COO})_2 \cdot 2\text{H}_2\text{O}$ (0.5 mmol each, totaling 2.5 mmol) were dissolved in 40 mL isopropanol under continuous stirring for 2 h. Then, 8 mL of glycerol was added to the mixture, and the resulting solution was stirred for an additional half-hour, forming a transparent pink solution. This solution was then transferred to a Teflon-lined stainless steel autoclave and kept at 180 °C for 10 h, as reported in our previous work [27]. The product NiMnZnMgCo-Glycerolate (HEG) was separated by centrifugation, washed with ethanol twice, and dried at 60 °C for 10 h. The sub-systems materials such as Ni-Glycerolate, NiMn-Glycerolate, and NiMnZn-Glycerolate (NiG, NiMnG, NiMnZnG, respectively) were prepared following the same approach. The respective porous oxide was obtained via annealing at 800 °C in the air for 3 h with a heating rate of 4 °C min⁻¹ in a tubular furnace OFT-1200X.

3.3. Preparation of Modified Carbon Paste Electrodes

The chemically modified carbon paste electrodes (CPEs) were prepared by exhaustively mixing electroactive materials (NiG, NiMnG, NiMnZnG, or HEG), graphite powder, and mineral oil in a mass ratio of 1:13.5:5.5 (about 5%, 57%, and 38% for each component, respectively) using a mortar and pestle in order to obtain homogeneously wet pastes. The resultant pastes were pressed firmly into the cavity of a 3.4 mm diameter Teflon tube (area = 0.09 cm²), which has a copper wire acting as an electrical connection. The surface of all modified CPEs was compacted by pressing the electrode onto a glass surface and then washed with distilled water. These protocols were also performed for the unmodified CPE.

3.4. Characterization

The materials were characterized by X-ray diffractometry (XRD) in a Bruker D8 Phaser diffractometer (Billerica, MA, USA) using Cu K α source ($\lambda = 1.5418 \text{ \AA}$, 40 kV, 40 mA, step = 0.05° with time steps of 1 s) in the 2 θ range from 5° to 90°. Infrared spectra were recorded in a Bruker ALPHA Fourier-transform infrared spectroscopy (FTIR) spectrophotometer (Billerica, MA, USA) using samples dispersed in KBr pellets.

The relative amounts of metals were measured via inductively coupled plasma optical emission spectroscopy (ICP-OES, Arcos/Spectro, Kleve, Germany) using concentrated dispersions of the as-prepared metal-glycerolates. Thermogravimetric analysis (TGA) was performed on a Shimadzu TGA Q500 instrument (Shimadzu, Kyoto, Japan) using synthetic air (80% N₂, 20% O₂) flux of 50 mL min⁻¹. Briefly, the analyzed material was placed in a platinum pan and equilibrated to 35 °C in the TGA before applying a heating ramp of 4 °C min⁻¹ up to 800 °C.

Chemical surface analyses of the microparticles were carried out by X-ray photoelectron spectroscopy (XPS), using a K-Alpha X-ray photoelectron spectrometer (Thermo Fisher Scientific, Waltham, MA, USA), equipped with a hemispherical electron analyzer and an Al K α microfocused monochromatized source with resolution of 0.1 eV. Survey (full range) and high-resolution spectra for carbon were acquired using a spot size of 400 μm and pass energy of 200 and 50 eV, respectively. The data were analyzed using the Thermo Avantage Software (Version 5.921).

3.5. Scanning Electron Microscope (SEM)

Scanning electron microscope (SEM) measurements were performed on a 5–15 kV Thermo Fisher Scientific Quanta 650 FEG (Waltham, MA, USA). The SEM measurements for the synthesized metal-glycerolates were performed using an accelerating voltage of usually 5.0 kV and a working distance of 10 mm. Energy dispersive spectroscopy (EDS) was performed using a Thermo Fisher Scientific Quanta 650 FEG with a FEG Schottky emission gun operated at 15 kV, equipped with an Oxford X-max 100TLE windowless X-ray detector.

3.6. Electrochemical Properties

Cyclic voltammetry (CV), Linear sweep voltammetry (LSV), Electrochemical impedance spectroscopy (EIS), and Chronoamperometry measurements were carried out using an EcoChemie Autolab PGSTAT30 potentiostat/galvanostat (Utrecht, The Netherlands) and a conventional three-electrodes cell, constituted by the modified CPE working electrode, an Ag/AgCl (3.0 mol L $^{-1}$ in KCl) reference, and a platinum wire as the counter electrode. The potential was converted from Ag/AgCl to RHE by Equation (1), where $E^0_{(\text{Ag}/\text{AgCl})}$ corresponds to 0.197 V at 25 $^{\circ}\text{C}$:

$$E_{\text{RHE}} = E_{\text{Ag}/\text{AgCl}} + E^0_{(\text{Ag}/\text{AgCl})} + 0.0059 \text{ pH}. \quad (1)$$

LSV measurements (sweep rate of 5 mV s $^{-1}$) were performed from 0 to 1 V vs. Ag/AgCl without iR correction. The overpotential (η_{10}) was calculated at a current density of 10 mA cm $^{-2}$, according to the Equation (2):

$$\eta_{10} = E_{\text{RHE}} (\text{at } 10 \text{ mA cm}^{-2}) - 1.23 \text{ V}. \quad (2)$$

AC impedance (with AC amplitude of 10 mV) experiments were executed at a potential of 1.573 V (vs. RHE) from 0.01 to 10 6 Hz. CV studies over 1000 cycles were registered from 0 to 0.6 V (vs. Ag/AgCl) with a scan rate of 100 mV s $^{-1}$.

4. Conclusions

Various metal-glycerolates have been synthesized in the present work using a one-step solvothermal method. Subsequently, the electroactivity of a high-entropy configuration containing Ni, Zn, Mn, Mg, and Co, along with their low-entropy counterparts, was evaluated toward OER. Introducing Mn and Zn ions in equimolar amounts leads to an increase in overpotential by about 31 mV when compared to NiG ($\eta_{10} = 310$ mV). This value is very similar to that of the HEG. This occurs due to the high amount of Mn and Zn ions, which favors the formation of the respective MnOOH and ZnOOH phases instead of providing a doping effect to the Ni $^{\text{II}}$ /Ni $^{\text{III}}$ redox couple in order to enhance the electronic properties of NiOOH species. Additionally, for the HEG, the poor electroactivity of Mg ions could be the reason for not surpassing the performance of NiG. Therefore, these findings shed light on the importance of favoring the presence of nickel and cobalt precursors in a multimetallic electrocatalyst. Furthermore, only a few studies are focused on using carbon paste as a conductive platform. The remarkable performance of the NiG-based CPE highlights an interesting condition for overcoming the low conductivity of the metal-glycerolates.

Supplementary Materials: The following supporting information can be downloaded at <https://www.mdpi.com/article/10.3390/catal13101371/s1>: Figure S1: TGA curve of NiG and HEG, in the range of 35 to 800 °C with a heating rate of 4 °C min, in synthetic air; Figure S2: SEM-EDS analysis of NiG in two more different regions; Figure S3: SEM-EDS analysis of HEG microspheres; Figure S4: SEM-EDS images of NiMnZnG showing the high content of zinc and manganese; Figure S5: Survey spectra of NiG, NiMnZnG, and HEG, and their respective high-resolution XPS spectra for C 1s and O 1s components; Figure S6: Survey spectra of NiMnG, and their respective high-resolution XPS spectra; Figure S7: Progression of 1000-cycle CV curve of glycerolates modified CPE; Figure S8: XRD pattern of NiG, HEG, and their respective metal oxides obtained by thermal treatment at 800 °C; Figure S9: SEM images of NiO, and SEM-EDS mappings of NiO; Figure S10: LSV curves of glycerolates modified CPE collected at a scan rate of 5 mV s⁻¹ in 1.0 M KOH electrolyte after 100th, 500th, and 1000th redox cycles.

Author Contributions: Conceptualization, I.S.L., L.A., J.M.G. and R.S.-Y.; methodology, I.S.L. and J.M.G.; formal analysis, I.S.L., J.M.G., R.S.P. and T.G.R.; Resources, L.A. and R.S.-Y.; data curation, I.S.L., J.M.G. and R.S.P.; writing—review and editing, I.S.L., J.M.G., T.G.R., L.A. and R.S.-Y.; supervision L.A.; funding acquisition, L.A. and R.S.-Y. All authors have read and agreed to the published version of the manuscript.

Funding: This research was funded by I.S.L. (FAPESP 2022/04127-4). In addition, we thank the fellowship granted to J.M.G. (FAPESP 2020/06176-7), and FAPESP (grant numbers: 2018/16896-7 and projects 2017/13137-5), and the support from National Science Foundation DMR-2311104. As well as CNPq (grant numbers: 311847-2018-8 and project 465389/2014-7).

Data Availability Statement: The authors confirm that the data supporting the findings of this study are available within the article.

Acknowledgments: This work made use of Instruments in the Electron Microscopy Core (Research Resources Center, UIC). We thank Koiti Araki (Laboratório de Química Supramolecular e Nanotecnologia, IQ-USP) and SisNANO USP for using the TGA and FTIR spectroscopy facility. We also thank the Brazilian Nanotechnology National Laboratory—LNNano@CNPEM (Brazil) for the use of SEM and EDS-SEM facilities.

Conflicts of Interest: The authors declare that they have no known competing financial interests or personal relationships that could have appeared to influence the work reported in this paper.

References

1. Ting, N.-H.; Nguyen, T.X.; Lee, C.-H.; Chen, Y.-C.; Yeh, C.-H.; Chen, H.-Y.T.; Ting, J.-M. Composition-controlled high entropy metal glycerate as high-performance electrocatalyst for oxygen evolution reaction. *Appl. Mater. Today* **2022**, *27*, 101398. [[CrossRef](#)]
2. Gonçalves, J.M.; Martins, P.R.; Angnes, L.; Araki, K. Recent advances in ternary layered double hydroxide electrocatalysts for the oxygen evolution reaction. *New J. Chem.* **2020**, *44*, 9981–9997. [[CrossRef](#)]
3. Wang, C.; Zhang, Q.; Yan, B.; You, B.; Zheng, J.; Feng, L.; Zhang, C.; Jiang, S.; Chen, W.; He, S. Facet Engineering of Advanced Electrocatalysts Toward Hydrogen/Oxygen Evolution Reactions. *Nanomicro Lett.* **2023**, *15*, 52. [[CrossRef](#)]
4. Zhang, Z.; Liang, X.; Li, J.; Qian, J.; Liu, Y.; Yang, S.; Wang, Y.; Gao, D.; Xue, D. Interfacial Engineering of NiO/NiCo₂O₄ Porous Nanofibers as Efficient Bifunctional Catalysts for Rechargeable Zinc–Air Batteries. *ACS Appl. Mater. Interfaces* **2020**, *12*, 21661–21669. [[CrossRef](#)]
5. Wang, Y.; Tao, S.; Lin, H.; Wang, G.; Zhao, K.; Cai, R.; Tao, K.; Zhang, C.; Sun, M.; Hu, J.; et al. Atomically targeting NiFe LDH to create multivacancies for OER catalysis with a small organic anchor. *Nano Energy* **2021**, *81*, 105606. [[CrossRef](#)]
6. Liu, Y.; Ran, N.; Ge, R.; Liu, J.; Li, W.; Chen, Y.; Feng, L.; Che, R. Porous Mn-doped cobalt phosphide nanosheets as highly active electrocatalysts for oxygen evolution reaction. *Chem. Eng. J.* **2021**, *425*, 131642. [[CrossRef](#)]
7. Du, X.; Ding, Y.; Zhang, X. MOF-derived Zn–Co–Ni sulfides with hollow nanosword arrays for high-efficiency overall water and urea electrolysis. *Green Energy Environ.* **2023**, *8*, 798–811. [[CrossRef](#)]
8. Xu, S.; Li, M.; Wang, H.; Sun, Y.; Liu, W.; Duan, J.; Chen, S. High-Entropy Metal–Organic Framework Arrays Boost Oxygen Evolution Electrocatalysis. *J. Phys. Chem. C* **2022**, *126*, 14094–14102. [[CrossRef](#)]
9. Gonçalves, J.M.; Ruiz-Montoya, J.G. Emerging high-entropy coordination compounds and their derivatives for energy application. *J. Mater. Chem. A* **2023**, *11*, 20872–20885. [[CrossRef](#)]
10. Ede, S.R.; Luo, Z. Tuning the intrinsic catalytic activities of oxygen-evolution catalysts by doping: A comprehensive review. *J. Mater. Chem. A* **2021**, *9*, 20131–20163. [[CrossRef](#)]
11. Gonçalves, J.M.; Santos, É.A.; Martins, P.R.; Silva, C.G.; Zanin, H. Emerging medium- and high-entropy materials as catalysts for lithium-sulfur batteries. *Energy Stor. Mater.* **2023**, *63*, 102999. [[CrossRef](#)]

12. Ritter, T.G.; Phakatkar, A.H.; Rasul, M.G.; Saray, M.T.; Sorokina, L.V.; Shokuhfar, T.; Gonçalves, J.M.; Shahbazian-Yassar, R. Electrochemical synthesis of high entropy hydroxides and oxides boosted by hydrogen evolution reaction. *Cell Rep. Phys. Sci.* **2022**, *3*, 100847. [[CrossRef](#)]
13. He, B.; Zu, Y.; Mei, Y. Design of advanced electrocatalysts for the high-entropy alloys: Principle, progress, and perspective. *J. Alloys Compd.* **2023**, *958*, 170479. [[CrossRef](#)]
14. Gonçalves, J.M.; Hennemann, A.L.; Ruiz-Montoya, J.G.; Martins, P.R.; Araki, K.; Angnes, L.; Shahbazian-Yassar, R. Metal-glycerolates and their derivatives as electrode materials: A review on recent developments, challenges, and future perspectives. *Coord. Chem. Rev.* **2023**, *477*, 214954. [[CrossRef](#)]
15. Horn, M.; Horns, U. Alkoxides, metal. In *Kirk-Othmer Encyclopedia of Chemical Technology*; John Wiley & Sons, Inc.: Hoboken, NJ, USA, 2001. [[CrossRef](#)]
16. Phakatkar, A.H.; Gonçalves, J.M.; Zhou, J.; Ritter, T.G.; Tamadoni Saray, M.; Sorokina, L.V.; Amiri, A.; Angnes, L.; Shokuhfar, T.; Shahbazian-Yassar, R. Enhanced Bacterial Growth by Polyelemental Glycerolate Particles. *ACS Appl. Bio Mater.* **2023**, *6*, 1515–1524. [[CrossRef](#)]
17. Ooka, H.; Huang, J.; Exner, K.S. The Sabatier Principle in Electrocatalysis: Basics, Limitations, and Extensions. *Front. Energy Res.* **2021**, *9*, 654460. [[CrossRef](#)]
18. Wang, C.; Yan, B.; Chen, Z.; You, B.; Liao, T.; Zhang, Q.; Lu, Y.; Jiang, S.; He, S. Recent advances in carbon substrate supported nonprecious nanoarrays for electrocatalytic oxygen evolution. *J. Mater. Chem. A* **2021**, *9*, 25773–25795. [[CrossRef](#)]
19. Raza, M.; Inayat, A.; Abu-Jdayil, B. Crude Glycerol as a Potential Feedstock for Future Energy via Thermochemical Conversion Processes: A Review. *Sustainability* **2021**, *13*, 12813. [[CrossRef](#)]
20. Nguyen, T.X.; Su, Y.H.; Lin, C.C.; Ruan, J.; Ting, J.M. A New High Entropy Glycerate for High Performance Oxygen Evolution Reaction. *Adv. Sci.* **2021**, *8*, 2002446. [[CrossRef](#)] [[PubMed](#)]
21. Wang, M.; Jiang, J.; Ai, L. Layered Bimetallic Iron–Nickel Alkoxide Microspheres as High-Performance Electrocatalysts for Oxygen Evolution Reaction in Alkaline Media. *ACS Sustain. Chem. Eng.* **2018**, *6*, 6117–6125. [[CrossRef](#)]
22. Reinoso, D.M.; Damiani, D.E.; Tonetto, G.M. Zinc glycerolate as a novel heterogeneous catalyst for the synthesis of fatty acid methyl esters. *Appl. Catal. B* **2014**, *144*, 308–316. [[CrossRef](#)]
23. Dong, Z.; Zhang, W.; Xiao, Y.; Wang, Y.; Luan, C.; Qin, C.; Dong, Y.; Li, M.; Dai, X.; Zhang, X. One-Pot-Synthesized CoFe-Glycerate Hollow Spheres with Rich Oxyhydroxides for Efficient Oxygen Evolution Reaction. *ACS Sustain. Chem. Eng.* **2020**, *8*, 5464–5477. [[CrossRef](#)]
24. Larcher, D.; Sudant, G.; Patrice, R.; Tarascon, J.M. Some Insights on the Use of Polyols-Based Metal Alkoxides Powders as Precursors for Tailored Metal-Oxides Particles. *Chem. Mater.* **2003**, *15*, 3543–3551. [[CrossRef](#)]
25. Gomes, J.F.; Garcia, A.C.; Gasparotto, L.H.S.; de Souza, N.E.; Ferreira, E.B.; Pires, C.; Tremiliosi-Filho, G. Influence of silver on the glycerol electro-oxidation over AuAg/C catalysts in alkaline medium: A cyclic voltammetry and in situ FTIR spectroscopy study. *Electrochim. Acta* **2014**, *144*, 361–368. [[CrossRef](#)]
26. Gonçalves, J.M.; Lima, I.S.; Phakatkar, A.H.; Pereira, R.S.; Martins, P.R.; Araki, K.; Angnes, L.; Shahbazian-Yassar, R. What are the Tower’s method products: Metal-hydroxides or metal-glycerolates? *Mater. Charact.* **2023**, *196*, 112636. [[CrossRef](#)]
27. Gonçalves, J.M.; Ghorbani, A.; Ritter, T.G.; Lima, I.S.; Saray, M.T.; Phakatkar, A.H.; Silva, V.D.; Pereira, R.S.; Yarin, A.L.; Angnes, L.; et al. Multimetallic glycerolate as a precursor template of spherical porous high-entropy oxide microparticles. *J. Colloid Interface Sci.* **2023**, *641*, 643–652. [[CrossRef](#)]
28. Ding, S.; An, J.; Ding, Z.; Zou, Y.; Zhao, L. Micron-sized NiMn-glycerate solid spheres as cathode materials for all-solid-state asymmetric supercapacitor with superior energy density and cycling life. *Chem. Eng. J.* **2022**, *431*, 134100. [[CrossRef](#)]
29. Septiani, N.L.W.; Kaneti, Y.V.; Fathoni, K.B.; Kani, K.; Allah, A.E.; Yulianto, B.; Nugraha; Dipojono, H.K.; Alothman, Z.A.; Golberg, D.; et al. Self-Assembly of Two-Dimensional Bimetallic Nickel–Cobalt Phosphate Nanoplates into One-Dimensional Porous Chainlike Architecture for Efficient Oxygen Evolution Reaction. *Chem. Mater.* **2020**, *32*, 7005–7018. [[CrossRef](#)]
30. Huang, J.; Li, Y.; Zhang, Y.; Rao, G.; Wu, C.; Hu, Y.; Wang, X.; Lu, R.; Li, Y.; Xiong, J. Identification of Key Reversible Intermediates in Self-Reconstructed Nickel-Based Hybrid Electrocatalysts for Oxygen Evolution. *Angew. Chem.* **2019**, *131*, 17619–17625. [[CrossRef](#)]
31. Zhao, Z.; Lamoureux, P.S.; Kulkarni, A.; Bajdich, M. Trends in Oxygen Electrocatalysis of 3 d-Layered (Oxy)(Hydro)Oxides. *ChemCatChem* **2019**, *11*, 3423–3431. [[CrossRef](#)]
32. Foruzin, L.J.; Rezvani, Z.; Shishavan, Y.H.; Habibi, B. Ni₂Zn_{0.5}Fe-LDH modified carbon paste electrode as an efficient electrocatalyst for water oxidation in neutral media. *Int. J. Hydrogen Energy* **2018**, *43*, 150–160. [[CrossRef](#)]
33. Wang, H.; Feng, E.-M.; Liu, Y.-M.; Zhang, C.-Y. High-performance hierarchical ultrathin sheet-based CoOOH hollow nanospheres with rich oxygen vacancies for the oxygen evolution reaction. *J. Mater. Chem. A* **2019**, *7*, 7777–7783. [[CrossRef](#)]
34. Anantharaj, S.; Noda, S. Appropriate Use of Electrochemical Impedance Spectroscopy in Water Splitting Electrocatalysis. *ChemElectroChem* **2020**, *7*, 2297–2308. [[CrossRef](#)]
35. Samanta, R.; Panda, P.; Mishra, R.; Barman, S. IrO₂-Modified RuO₂ Nanowires/Nitrogen-Doped Carbon Composite for Effective Overall Water Splitting in All pH. *Energy Fuels* **2022**, *36*, 1015–1026. [[CrossRef](#)]
36. Zhang, T.; Huang, H.; Han, J.; Yan, F.; Sun, C. Manganese-Doped Hollow Layered Double (Ni, Co) Hydroxide Microcuboids as an Efficient Electrocatalyst for the Oxygen Evolution Reaction. *ChemElectroChem* **2020**, *7*, 3852–3858. [[CrossRef](#)]

37. Kaneti, Y.V.; Guo, Y.; Septiani, N.L.W.; Iqbal, M.; Jiang, X.; Takei, T.; Yulianto, B.; Alothman, Z.A.; Golberg, D.; Yamauchi, Y. Self-templated fabrication of hierarchical hollow manganese-cobalt phosphide yolk-shell spheres for enhanced oxygen evolution reaction. *Chem. Eng. J.* **2021**, *405*, 126580. [[CrossRef](#)]
38. Septiani, N.L.W.; Kaneti, Y.V.; Guo, Y.; Yulianto, B.; Jiang, X.; Ide, Y.; Nugraha, N.; Dipojono, H.K.; Yu, A.; Sugahara, Y.; et al. Holey Assembly of Two-Dimensional Iron-Doped Nickel-Cobalt Layered Double Hydroxide Nanosheets for Energy Conversion Application. *ChemSusChem* **2020**, *13*, 1645–1655. [[CrossRef](#)]
39. Moradi, M.; Hasanvandian, F.; Afshar, M.G.; Larimi, A.; Khorasheh, F.; Niknam, E.; Setayesh, S.R. Incorporation of Fe in mixed CoCu-alkoxide hollow sphere for enhancing the electrochemical water oxidation performance. *Mater. Today Chem.* **2021**, *22*, 100586. [[CrossRef](#)]
40. Enman, L.J.; Burke, M.S.; Batchellor, A.S.; Boettcher, S.W. Effects of Intentionally Incorporated Metal Cations on the Oxygen Evolution Electrocatalytic Activity of Nickel (Oxy)hydroxide in Alkaline Media. *ACS Catal.* **2016**, *6*, 2416–2423. [[CrossRef](#)]

Disclaimer/Publisher's Note: The statements, opinions and data contained in all publications are solely those of the individual author(s) and contributor(s) and not of MDPI and/or the editor(s). MDPI and/or the editor(s) disclaim responsibility for any injury to people or property resulting from any ideas, methods, instructions or products referred to in the content.